

Exploring superconductivity in dynamically stable carbon-boron clathrates trapping molecular hydrogen

Akinwumi Akinpelu, Mangladeep Bhullar, Timothy A. Strobel, and Yansun Yao

Citation: Chin. Phys. B, 2025, 34 (**3**): 036103. DOI: 10.1088/1674-1056/ada757
Journal homepage: http://cpb.iphy.ac.cn; http://iopscience.iop.org/cpb

What follows is a list of articles you may be interested in

Pressure-induced superconductivity and phase transition in PbSe and PbTe

Yuyang Jiang(江宇阳), Cuiying Pei(裴翠颖), Qi Wang(王琦), Juefei Wu(吴珏霏), Lili Zhang(张丽丽), Chao Xiong(熊超), and Yanpeng Qi(齐彦鹏)
Chin. Phys. B, 2024, 33 (**12**): 126105. DOI: 10.1088/1674-1056/ad8ecc

Valence electron structures dependences of structural stability and properties of REX_3(*RE*=rare earth; *X*=In, Tl) and *RE*(In, Co)$_3$ alloys

Boyang Li(李博洋), Yongquan Guo(郭永权), Yi-Chen Feng(冯奕晨), Xinze Wang(王鑫泽), and Wei Liu(刘葳)
Chin. Phys. B, 2024, 33 (**11**): 116102. DOI: 10.1088/1674-1056/ad7575

Pressure-induced structural, electronic, and superconducting phase transitions in $TaSe_3$

Yuhang Li(李宇航), Pei Zhou(周佩), Chi Ding(丁驰), Qing Lu(鲁清), Xiaomeng Wang(王晓梦), and Jian Sun(孙建)
Chin. Phys. B, 2024, 33 (**10**): 106102. DOI: 10.1088/1674-1056/ad6f92

Pressure-induced stable structures and physical properties of Sr-Ge system

Shuai Han(韩帅), Shuai Duan(段帅), Yun-Xian Liu(刘云仙), Chao Wang(王超), Xin Chen(陈欣), Hai-Rui Sun(孙海瑞), and Xiao-Bing Liu(刘晓兵)
Chin. Phys. B, 2023, 32 (**1**): 016101. DOI: 10.1088/1674-1056/ac6db5

Structural evolution and molecular dissociation of H_2S under high pressures

Wen-Ji Shen(沈文吉), Tian-Xiao Liang(梁天笑), Zhao Liu(刘召), Xin Wang(王鑫), De-Fang Duan(段德芳), Hong-Yu Yu(于洪雨), and Tian Cui(崔田)
Chin. Phys. B, 2022, 31 (**7**): 076102. DOI: 10.1088/1674-1056/ac5980

SPECIAL TOPIC — Structures and properties of materials under high pressure

Exploring superconductivity in dynamically stable carbon–boron clathrates trapping molecular hydrogen

Akinwumi Akinpelu[1], Mangladeep Bhullar[1], Timothy A. Strobel[2,†], and Yansun Yao[1,‡]

[1] *Department of Physics and Engineering Physics, University of Saskatchewan, Saskatoon, Saskatchewan, S7N 5E2, Canada*
[2] *Earth and Planets Laboratory, Carnegie Institution for Science, 5241 Broad Branch Road, Northwest, Washington DC 20015, USA*

(Received 28 November 2024; revised manuscript received 5 January 2025; accepted manuscript online 8 January 2025)

The recent discovery of type-VII boron–carbon clathrates with calculated superconducting transition temperatures approaching ∼ 100 K has sparked interest in exploring new conventional superconductors that may be stabilized at ambient pressure. The electronic structure of the clathrate is highly tunable based on the ability to substitute different metal atoms within the cages, which may also be large enough to host small molecules. Here we introduce molecular hydrogen (H_2) within the clathrate cages and investigate its impact on electron–phonon coupling interactions and the superconducting transition temperature (T_c). Our approach involves combining molecular hydrogen with the new diamond-like covalent framework, resulting in a hydrogen-encapsulated clathrate, $(H_2)B_3C_3$. A notable characteristic of $(H_2)B_3C_3$ is the dynamic behavior of the H_2 molecules, which exhibit nearly free rotations within the B–C cages, resulting in a dynamic structure that remains cubic on average. The static structure of $(H_2)B_3C_3$ (a snapshot in its dynamic trajectory) is calculated to be dynamically stable at ambient and low pressures. Topological analysis of the electron density reveals weak van der Waals interactions between molecular hydrogen and the B–C cages, marginally influencing the electronic structure of the material. The electron count and electronic structure calculations indicate that $(H_2)B_3C_3$ is a hole conductor, in which H_2 molecules donate a portion of their valence electron density to the metallic cage framework. Electron–phonon coupling calculation using the Migdal–Eliashberg theory predicts that $(H_2)B_3C_3$ possesses a T_c of 46 K under ambient pressure. These results indicate potential for additional light-element substitutions within the type-VII clathrate framework and suggest the possibility of molecular hydrogen as a new approach to optimizing the electronic structures of this new class of superconducting materials.

Keywords: superconductivity, electronic structure, density functional theory, molecular dynamics

PACS: 61.50.Ah, 71.20.–b, 74.20.Pq, 74.25.–q

DOI: 10.1088/1674-1056/ada757 **CSTR:** 32038.14.CPB.ada757

1. Introduction

Superconductivity is a quantum phenomenon where a material exhibits zero electrical resistance and simultaneously expels magnetic fields when cooled below a certain critical temperature (T_c).[1] Superconductors have remarkable implications for next-generation technologies, including low-loss electrical transmission, computer chips and advanced medical imaging. Although superconductors have been known since 1911[2] and are currently employed in various industries such as MRI imaging and magnetic levitation devices, their widespread application faces a significant obstacle due to the necessity of maintaining extremely low temperatures to sustain the superconducting state. The current record of T_c at one atmosphere is around 137 K, held by 'unconventional' cuprate materials,[3] which is practically too low for widespread use. On the other hand, recent research has seen a breakthrough in finding high-T_c superconductivity in several hydrogen-rich materials under extreme pressures. For instance, hydrogen sulfide (H_3S) exhibits a measured T_c of around 203 K under compression to 155 GPa,[4–6] while lanthanum hydride (LaH_{10}) demonstrates an even higher T_c ranging from 250 K to 260 K at 170–180 GPa.[7–10] For superhydrides, experiments suggest that they are conventional, or BCS,[11] superconductors described by the electron–phonon coupling (EPC) mechanism.[12,13] Theoretical predictions within the BCS framework indicate the existence of numerous high-pressure superhydrides with T_c values close to or surpassing room temperature,[14–16] and experimental efforts are ongoing to validate these predictions.[17] On the other hand, the superhydrides formed under extreme pressures (generally above 150 GPa) are thermodynamically unstable and decompose at lower pressures, limiting their practical applications. For this reason, attention is gradually shifting towards developing superconducting materials capable of sustaining relatively high T_c values while remaining stable at near ambient pressures.

Migdal–Eliashberg theory, an extension of the BCS theory to the strong coupling regime, suggests that compounds composed of light elements are good candidates for conven-

†Corresponding author. E-mail: tstrobel@carnegiescience.edu
‡Corresponding author. E-mail: yansun.yao@usask.ca

© 2025 Chinese Physical Society and IOP Publishing Ltd. All rights, including for text and data mining, AI training, and similar technologies, are reserved.

tional superconductors.[18,19] Other than the apparent choice of hydrogen,[20] compounds containing boron and carbon are frequently sought after, as their strong covalent bonds are expected to offer enhanced stability for recovery under ambient conditions. MgB_2, for example, exhibits the highest known T_c (39 K) among conventional superconductors at atmospheric pressure,[21] once believed to represent the theoretical upper limit for T_c (known as the 'McMillian limit'[22]) in conventional superconductors. Recently, carbon-based clathrates have been suggested as potential candidates for conventional superconductors with very high T_cs.[23–25] In particular, the Na-filled carbon clathrate NaC_6 is predicted to have a T_c as high as 119 K at atmospheric pressure, in which the high symmetry sp^3 network is expected to induce strong EPC.[26] Additionally, Ga and Ge-filled carbon clathrates, GaC_6 and GeC_6, are predicted to be dynamically stable at ambient pressure, with the calculated T_c values near or above the boiling point of liquid nitrogen (77 K).[27] However, despite a clear analogy to silicon clathrates, laboratory synthesis of carbon clathrates remains elusive, primarily due to significant formation energies and uncertain synthetic pathways. On the other hand, density functional calculations suggest that carbon clathrates could be stabilized by substituting some carbon atoms with boron, leveraging boron's electron-deficient bonding to strengthen the cages.[28] This idea has led to the synthesis of a Sr-filled boron–carbon clathrate, SrB_3C_3.[29] SrB_3C_3 can be synthesized near 50 GPa and quench-recovered to ambient conditions under an inert atmosphere. SrB_3C_3 has a bipartite sodalite structure consisting of interconnected truncated octahedral B–C cages arranged in a body centered cubic (bcc) lattice, each hosting an Sr atom. This structure is the borocarbide analogue to clathrate hexahydrides (such as CaH_6) and behaves as a hole conductor due to partially filled conduction bands. Experimentally, the superconducting transition of SrB_3C_3 was observed at approximately 20 K at 40 GPa, but its T_c was estimated to approach that of MgB_2 at ambient pressure.[30] The hole-doped SrB_3C_3 is predicted to have a T_c above 77 K.[31]

The synthesis of SrB_3C_3 clathrate has stimulated many interesting studies. This structure's guest–host nature allows for guest substitution and doping to fine-tune the electronic structure. Shortly thereafter, LaB_3C_3 was synthesized and quenched to ambient conditions, but it functions as a semiconductor due to filled conduction bands.[32] CaB_3C_3 and BaB_3C_3 were predicted to be BCS superconductors with $T_c \leq$ 50 K at moderate or ambient pressures.[33,34] Binary-guest clathrates, such as XYB_6C_6, where X and Y metals are chosen to achieve a desired level of hole/electron doping, have been shown to have a significantly increased T_c compared to their mono-guest counterparts.[34–37] For instance, $RbYbB_6$ and $RbBaB_6C_6$ have calculated T_c values close to 70 K at ambient pressure,[36] while $KPbB_3C_3$ is predicted to possess the highest T_c at ambient pressure within this group, reaching 88 K, surpassing the boiling point of liquid nitrogen.[37] In silicon analogs, RbB_3Si_3 is predicted to be metastable at one atmosphere with an estimated T_c of 14 K.[38] Furthermore, with a varied B/C ratio, compounds XB_2C_8 (X = K, Rb, Cs, Sr, Ba, Ga, In, Tl, Sn, Pb, and Bi) are predicted to be stable at ambient pressure, all exhibiting calculated T_c above 77 K.[39]

Given the size of the truncated octahedral cages within the B–C clathrate, it is potentially feasible to fill them with the lightest element, hydrogen. Utilizing hydrogen will likely induce high-frequency phonons and strong EPC, leading to phonon-mediated, high-T_c superconductivity.[4] Hydrogen could potentially be added via covalently bound defects within the clathrate framework structure, or as molecular entities within the cages.[41] In this article, we propose combining H_2 molecules with the sodalite B_3C_3 framework to create a novel clathrate $(H_2)B_3C_3$. Through theoretical research, we investigated multiple $(H_2)B_3C_3$ clathrates with H_2 as a guest incorporated into the cages of the B_3C_3 host structures. Our results show that each cage can only accommodate one freely rotating H_2 molecule, with interactions between H_2 and the cages being of the van der Waals type, inherently weak in nature. The $(H_2)B_3C_3$ solid is predicted to be dynamically stable at ambient pressure while thermodynamically metastable. The EPC calculations for static $(H_2)B_3C_3$ in the $P4_2/mmc$ space group indicate phonon-mediated superconductivity with an estimated T_c of 40–48 K at ambient and near-ambient pressure. These findings provide guidance for tuning the electronic structures of carbon–boron clathrate materials and underscore the importance of further investigations on clathrate-based superconductors.

2. Computational details

Structural relaxations and electronic structure calculations were performed in the framework of density functional theory (DFT)[42,43] within the Perdew–Burke–Ernzerhof (PBE)[44] functional and plane-wave basis set as implemented in the Vienna *Ab Initio* Simulation Package (VASP).[45] Dispersion interactions were accounted for using nonlocal optB88-vdW density functional.[46] The projector augmented wave (PAW) potentials[47] were used, with H, B, and C atoms treated with $1s^1$, $2s^22p^1$, and $2s^22p^2$ valence states, respectively. Dense k-point meshes with a spacing of 0.2 $Å^{-1}$ were employed to sample the first Brillouin zone (BZ) to ensure convergence of energies to within 5 meV/atom in electronic calculations.

The Car–Parrinello molecular dynamics (CPMD) simulations[48] were performed on a supercell comprising 128 atoms using the Quantum ESPRESSO package,[49] employing norm-conserving pseudopotentials[5] and an energy cutoff of 70 Rydberg. A fictitious electron mass of 50 a.u. was

used to integrate the ionic motions, with a time step of 1 fs to accurately capture the high-frequency motions of hydrogen. The simulation cell adopted a supercell of the optimized structure at 0 GPa and 0 K. Structural stability of the supercell was examined over 20 ps in an isothermal-isobaric (NPT) ensemble subsequent to an initial 3-ps temperature equilibration in a canonical (NVT) ensemble. The temperature in the CPMD calculations was controlled by a Nosé thermostat.[51] Topological analysis of the charge density was performed using the quantum theory of atoms in molecules (QTAIM).[52] Dynamical stabilities of the predicted structures were evaluated using phonon dispersion and phonon density of states, calculated with density functional perturbation theory (DFPT),[53] as implemented in VASP and postprocessed with the PHONOPY code.[54] The EPC properties were calculated using the linear response theory within the Quantum ESPRESSO package. The EPC matrices were evaluated in the first BZ on a $4\times4\times4$ q-grid with individual EPC matrices obtained with a $16\times16\times16$ k-grid and a Gaussian smearing width of 0.05 Ry. The superconducting critical temperature T_c was estimated using the Allen–Dynes-modified McMillan equation[55,56] with renormalized Coulomb potential $\mu^* = 0.10$. Crystal structures were visualized using the Visualization for Electronic Structural Analysis (VESTA) tool.[57]

3. Results and discussion

Exhaustive structure searches were carried out for H–B–C clathrate structures at 0 and 2 GPa. A $2\times2\times2$ supercell of B_3C_3 clathrate (96 atoms) was used as the host structure, which has 16 distinct cages for the guest enclosure. A varying number of H_2 molecules (ranging from 1 to 4) with randomly assigned orientations were introduced into each cage of the host structure and subsequently optimized. The stability analysis of the optimized structures shows that the B_3C_3 clathrate structure can accommodate only one H_2 molecule within each cage. The absence of H_2 molecules will lead to the collapse of cages, as indicated by strongly imaginary frequencies throughout the first Brillouin zone. Similarly, the structure with half of the molecular hydrogen removed collapses due to the imbalance in the volume and size of the cages.

In contrast, the presence of multiple H_2 molecules causes the breakdown of their molecular structures and the consequential formation of covalent bonding with the cage walls. Interestingly, the energies of stable structures appear insensitive to the orientation of the H_2 molecules, suggesting relatively weak van der Waals-type interactions between H_2 molecules and the cages. Nevertheless, these weak interactions are capable of stabilizing the $[B_3C_3]^{3-}$ cages. Further molecular dynamics investigation (see later) shows that at room temperature, H_2 molecules exhibit free rotation within the cages without any preferred orientations while the host clathrate structure remains rigid.

The static structure with the lowest energy at both 0 GPa and 2 GPa has a tetragonal unit cell in the $P4_2/mmc$ space group, featuring the $(H_2)B_3C_3$ stoichiometry (Fig. 1(a)). This structure represents an energetically favored instantaneous configuration within the dynamic structure. In this structure, B and C atoms combine to form truncated octahedral cages with six four-sided faces and eight six-sided faces, which are interconnected into a three-dimensional host framework (Fig. 1(b)). Each cage comprises 24 vertices with alternating C and B atoms and encloses an H_2 molecule at the center. All hydrogen molecules have the same orientation, aligned with a major (z) axis of the cages. Consequently, due to this hydrogen alignment, the cages experience slight elongation along the z-axis, inducing a tetragonal distortion in the unit cell. At 0 GPa, the optimized structural parameters for the $P4_2/mmc$ structure are: H $4i$ 0.0, 0.5, 0.072; B1 $4j$ 0.78, 0.0, 0.0; B2 $2f$ 0.5, 0.5, 0.25; C1 $4k$ 0.719, 0.5, 0.5, and C2 $2e$ 0.0, 0.0, 0.25 with $a = 4.6$ Å and $c = 5.14$ Å. While dynamically stable, the calculated formation energy of this structure with respect to the elements (B, C, and H_2 solids) is found to be +402 meV/atom at ambient pressure, indicating an energetic preference for chemical disproportionation. The calculated formation energy decreases under high pressure, specifically to +395 meV/atom at 5 GPa and +309 meV/atom at 10 GPa. This suggests that the likelihood of synthesis improves under high-pressure conditions.

To investigate the stability of the H–B–C clathrate, CPMD simulations were performed on a supercell of the $P4_2/mmc$ structure at room temperature (300 K) and atmospheric pressure. The time evolution of the structure was monitored over 20-ps NPT trajectories following a 3-ps temperature equilibration in an NVT ensemble. The variations in total energy, pressure, temperature, and lattice constants as functions of time in both NPT and NVT ensembles are presented in the supporting information (Figs. S1–S3). The thermal trajectory (Fig. 1(d)) reveals that H_2 molecules undergo apparently free rotation within the clathrate cages, as indicated by the near-spherical shape of the trajectory profile. In contrast, the B and C atoms exhibit much smaller thermal motions about their crystallographic sites, effectively keeping the cages rigid. The rotational freedom of H_2 molecules implies an extensive sampling of many possible structures with no preferred orientations, thereby preserving an average cubic cell structure. The transition from a tetragonal to a cubic cell can be observed in the time evolution of the lattice constants within the NPT ensemble (Figs. S2(a) and S2(b)). The tetragonal distortion, as observed in the static structure (Fig. 1(c)), is smeared out in the dynamics structure (Fig. 1(d)). The rotation of H_2 molecules is also a structural feature of the low-pressure

phase I of solid bulk hydrogen that is stable up to pressures of about 110 GPa.[58] Consequently, we calculated the energy barrier according to the rotation of the molecular hydrogen at 0 GPa using the method described in Ref. [59]. The rotational barrier peaks midway through the rotation, which is found to be 0.0203 eV/atom (Table S1). This low energy barrier[60] indicates that the molecular hydrogen in the $(H_2)B_3C_3$ can rotate freely in the cage at moderate temperatures, i.e., room temperature. Within the MD trajectories, the H–B–C clathrate appears to be stable at room temperature and atmospheric pressure, without signs of hydrogen diffusion. The interactions between H_2 molecules and the host structure are significantly influenced by their dynamic behavior.

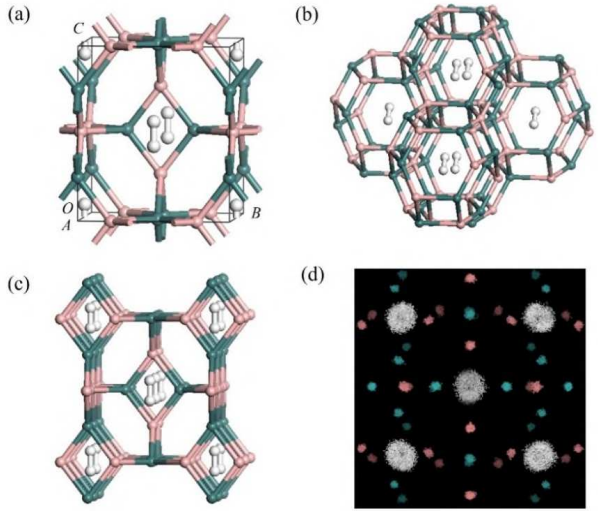


Fig. 1. (a) The unit cell of $(H_2)B_3C_3$ structure in the $P4_2/mmc$ space group. (b) and (c) Different perspective views of the $(H_2)B_3C_3$ structure. (d) Depicted thermal trajectories of $(H_2)B_3C_3$ obtained from NPT CPMD simulations at 300 K and atmospheric pressure. The H, B, and C atoms are colored white, pink, and cyan, respectively.

Another measure of the stability of the H–B–C clathrate is the dynamic stability of the static structure. Phonon dispersion curves for the $P4_2/mmc$ structure were calculated at 0 K and atmospheric pressure, as shown in Fig. 2(a). The absence of imaginary frequencies in the entire first Brillouin zone shows that the structure is dynamically stable, which connotes the possible fabrication of this material under suitable conditions. Notably, the phonon dispersion curves feature high-frequency H–H vibrons exceeding 140 THz, which surpasses the nominal vibrational frequency of free H_2 molecules. This observation suggests that the H–H bonds in the H_2 molecules within the H–B–C clathrate are strengthened by the enclosure provided by the B–C cage. The calculated H–H bond length in the H–B–C clathrate is 0.72 Å at atmospheric pressure, shorter than the ambient bond length in an H_2 molecule (0.74 Å). One can infer that the reduction in bond length is due to the compression by the cages. The electron topology analysis subsequently indicates that despite the compression of the bond by the surrounding cages, there is a partial electron depletion from the bonding orbital of the H_2 molecule, suggesting a partial transfer of charge from H_2 to the cages.[61] The lack of dispersion in the high-frequency vibrations also suggests minimal interactions between the H_2 molecules and the cages, consistent with the dynamics revealed in CPMD trajectories. Vibrations of the B–C framework dominate the mid- and low-frequency phonons. In particular, the acoustic modes are entirely contributed to by the B–C framework. The calculations at 2 GPa reveal very similar phonon dispersion (Fig. 2(b)), suggesting little changes in the interactions between the H_2 units and B–C framework to occur in this pressure range. Additional phonon calculations were performed at 5 GPa and 10 GPa. At 5 GPa, the phonon dispersions reveal an absence of imaginary frequencies (Fig. S4), indicating dynamical stability. At 10 GPa, the phonons remain primarily stable, but a slight imaginary mode starts to develop around the zone center (Fig. S4b). This indicates that $(H_2)B_3C_3$ is estimated to be dynamically stable up to nearly 10 GPa. At much higher pressures, the compression induces bonding between hydrogen and the B–C cages, leading to the collapse of the clathrate structure and the formation of unstable hydrides.

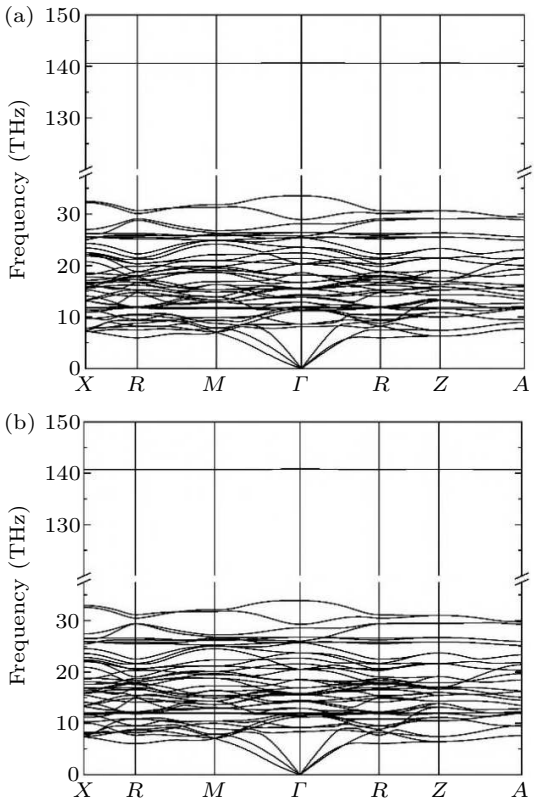


Fig. 2. Phonon dispersion curves for $(H_2)B_3C_3$ clathrate calculated (a) at atmospheric pressure and 0 K, and (b) at 2 GPa and 0 K. Axis breaks are added to the *y*-axis to increase the visible regions of the graphs.

The electronic band structures depicted in Figs. 3(a) and 3(b) demonstrate the metallic nature of the $(H_2)B_3C_3$ clathrate. Within $(H_2)B_3C_3$, the B–C cages exhibit strong covalent bonding between sp^3 hybridized B and C atoms while only interacting weakly with the freely rotating H_2 molecules. The weak interactions result in the H_2 molecule transferring only a mini-

mal amount of electrons to the B–C cages, thereby facilitating the formation of a hole conductor, as evidenced by the band structure. Bader's net atomic charge was computed to understand the net charge distribution within the cage. The results indicate an average transfer of approximately 0.053 e^- per hydrogen atom to the B–C cages under ambient pressure conditions. Polar bonds are formed within the cages due to the disparate electronegativities between the B and C atoms (0.51 difference on the Pauling scale), as revealed by the net positive charge on the B atom (+0.167/atom) and net negative charge on the C atom (−1.48/atom) in Bader's analysis.

At ambient pressure, the shortest B–H and C–H distances are 2.43 Å in $(H_2)B_3C_3$ clathrate. These distances are far surpassing the typical B–H σ bond length of 1.19 Å (as seen in BH_3) and C–H σ bond length of 1.09 Å (as seen in CH_4), suggesting the absence of bonding interactions between the H_2 molecules and the cages. On the other hand, the nearest H–H distance is 0.72 Å, which is comparable to the H–H bond length of 0.74 Å in molecular hydrogen. At a slightly higher pressure of 2 GPa, these distances are marginally reduced to 2.42 Å, 2.42 Å, and 0.72 Å, respectively. This bonding environment within the $(H_2)B_3C_3$ clathrate is depicted through the electron localization function (ELF)[62] isosurface (Fig. A1) computed with $\eta = 0.75$. The ELF isosurface in the $(H_2)B_3C_3$ cage-like structure exhibits a perfect overlap of the electron clouds of hydrogen atoms, indicating covalent bonding within the H_2 units as confirmed by the high-frequency phonon modes. Also, localized electron pairs exist between B and C atoms, indicating B–C bonding within the cages. Notably, there is no electron localization between H and the B–C cages, suggesting that any interaction between hydrogen and the cages in this material should be closed-shell in nature, consistent with van der Waals (vdW) interactions.

The quantum QTAIM analysis[63] identifies bond critical points (BCPs) in the interatomic regions between distinct H···H, H···C, and B···C atoms (Tables A1 and A2). The calculated values of electron density, denoted as $\rho(\boldsymbol{r}_{\mathrm{BCP}})$, and the Laplacian $\nabla^2\rho(\boldsymbol{r})$ at the BCPs along H···C paths are 0.116 $e^-\cdot$Å^{-3} and 1.476 $e^-\cdot$Å^{-5}, respectively. $\nabla^2\rho(\boldsymbol{r})$ needs to be positive in the context of H···C interactions, as these interactions primarily involve the contraction of electrons away from the interatomic region toward each nucleus, leading to a local minimum in electron density at the BCP.[64] This characterization of the Laplacian defines closed-shell interactions between H and its nearest neighboring C atoms, which, combined with low electron density $\rho(\boldsymbol{r}_{\mathrm{BCP}})$, suggests van der Waals (vdW) type interactions. For comparison, the conventional hydrogen bonds have $\rho(\boldsymbol{r}_{\mathrm{BCP}})$ up to 0.24 $e^-\cdot$Å^{-3}.[65,66] The calculated $\rho(\boldsymbol{r}_{\mathrm{BCP}})$ at 0 GPa for H···H BCPs is 2.001 Å^{-3} with negative Laplacian (−41.105 $e^-\cdot$Å^{-5}), indicating strong covalent bonding where electron density peaks at $\boldsymbol{r}_{\mathrm{BCP}}$. At the same time, the calculated $\rho(\boldsymbol{r}_{\mathrm{BCP}})$ between B···C atoms are 1.035 Å^{-3}, 1.026 Å^{-3}, and 0.761 Å^{-3}, respectively, for the three nearest neighboring B···C paths, with corresponding negative Laplacian values of −2.624 $e^-\cdot$Å^{-5}, −3.714 $e^-\cdot$Å^{-5}, and −4.842 $e^-\cdot$Å^{-5} at their respective BCPs. Under pressure, the values of $\rho(\boldsymbol{r}_{\mathrm{BCP}})$ increase slightly because of bond shortening, resulting in values of 0.118 $e^-\cdot$Å^{-3} and 2.004 $e^-\cdot$Å^{-3} at 2 GPa between distinct H···C and H···H atoms, respectively (Table A2). Similarly, $\rho(\boldsymbol{r}_{\mathrm{BCP}})$ values of 1.041 $e^-\cdot$Å^{-3}, 1.033 $e^-\cdot$Å^{-3} and 0.769 $e^-\cdot$Å^{-3} are calculated for the three B–C paths, respectively. Regarding the interaction strength, the dissociation energy (E_{BD}) for H···C interactions is only 15.27 kJ·mol^{-1}, which is approximately 4% of the dissociation energy for an H–C covalent bond ($\sim$ 390 kJ·mol^{-1}), signifying very weak vdW interactions. In contrast, the E_{BD} for B–C and H–H interactions ranges from 176.22 kJ·mol^{-1} to 807.26 kJ·mol^{-1}, indicating intermediate to strong covalent bonds (Table A1).

At 0 GPa (Fig. 3(a)), a pseudogap occurs at 4.2 eV above the Fermi level, which separates the bands formed by bonding and antibonding orbitals of the B–C cages. This phenomenon is attributable to approximately three unfilled valence bands, accounting for the absence of 6 bonding electrons within the B–C clathrate. Increasing the pressure to 2 GPa (Fig. 3(b)) strengthens the orbital overlap in the B–C clathrate, which stabilizes bonding interactions while destabilizing antibonding interactions, thereby increasing the overall bandwidth.[67] This moderate expansion in bandwidth brings valence and conduction bands closer, diminishing the pseudogap. The band structures also indicate the existence of a small flat band section next to the steep sections in two bands near the Fermi level (E_{f}), particularly around the R symmetry point. This is interesting in raising the likelihood of the Cooper pairs formation in $(H_2)B_3C_3$. Previous theories suggest that this is a favorable condition for enhancing the chance of EPC and superconductivity.[68] $(H_2)B_3C_3$ emerges as a good candidate for phonon-mediated superconductivity under ambient conditions. As shown in Fig. 3(a), the projected density of states (pDOS) for the $(H_2)B_3C_3$ clathrate confirms its metallic nature with a relatively low DOS at the Fermi level, i.e., 0.715 states/eV/$(H_2)B_3C_3$, under ambient pressure conditions. The contribution of H_2 states to the DOS at the Fermi level is minimal, accounting for only 0.00711 states/eV/$(H_2)B_3C_3$, or 1%, with the majority of the H_2 states located below the Fermi level down to −0.87 eV. The bandwidth of the H_2 states is consistent with that of molecular H_2. Due to the minimal amount of electron transfer from H_2 to the B–C cages, the B_3C_3 unit lacks almost three electrons from achieving a balanced electron count, resulting in the formation of a hole conductor. In contrast, in SrB_3C_3, the divalent Sr^{2+} can transfer two electrons to the B–C cages, leading to a less depleted

hole conductor with a lower DOS at the Fermi level compared to $(H_2)B_3C_3$.[29] In the extreme case of LaB_3C_3, the electrons transferred from trivalent La fully populate the bands of the B–C cages, resulting in an insulating (semiconducting) material.[32] The relatively low DOS at the Fermi level in B_3C_3-based clathrates is primarily attributed to the steep slope of most energy bands crossing the Fermi level due to strong B–C bonds in the cages, indicating fewer flat dispersions near the E_f. On the other hand, several flat bands are observed in fcc-LaH_{10} and shallow-sloped bands in hcp-CeH_9, contributing to their high DOS at E_f. The pDOS depicted in Figs. 3(a) and 3(b) suggest that carbon p orbitals make the most substantial contributions to the total DOS close to the E_f. The orientation of H_2 was changed by 90° to investigate its effect on the electronic properties of the clathrate at 0 GPa. A pseudogap is observed above the Fermi level as well (Fig. S6). The pDOS for the $(H_2)B_3C_3$ clathrate confirms its metallic nature with a relatively low DOS at the Fermi level under ambient pressure conditions. The contribution of H_2 states to the DOS at the Fermi level remaines minimal, and the majority of the H_2 states are located below the Fermi level.

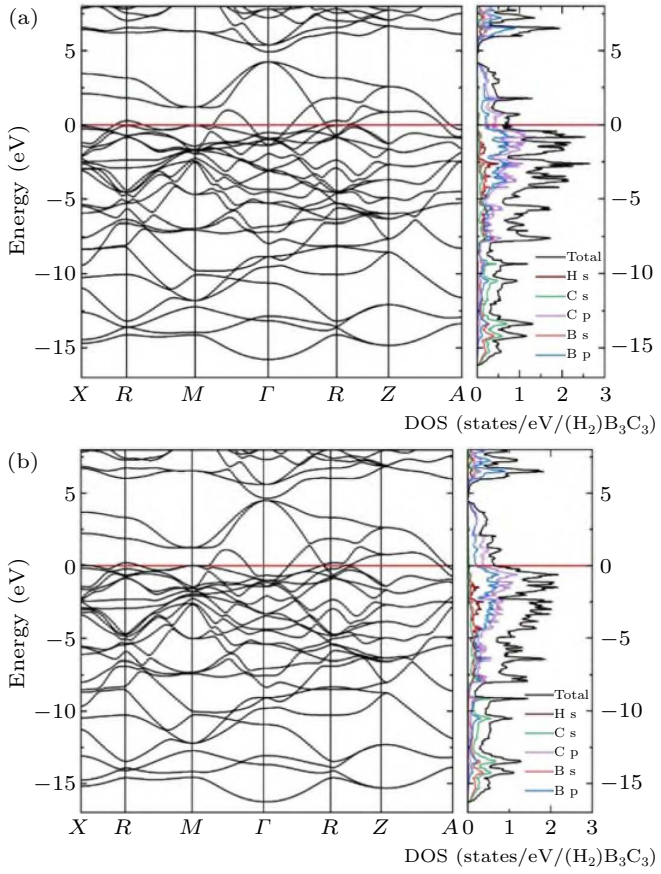


Fig. 3. Electronic band structure and orbital-projected density of states (pDOS) for $(H_2)B_3C_3$ clathrate calculated (a) at atmospheric pressure, and (b) at 2 GPa.

To investigate potential superconductivity in $(H_2)B_3C_3$, we calculated the EPC properties and estimated the superconducting T_c by the Allen–Dynes modified McMillan equation[56]

$$T_c = \frac{\omega_{log}}{1.20} \exp\left(-\frac{1.04(1+\lambda)}{\lambda - \mu^*(1+0.62\lambda)}\right), \quad (1)$$

where ω_{log} is the logarithmic average of phonon frequencies, and λ is the EPC parameter representing the (averaged) strength of the electron–phonon coupling in the lattice. In the realm of weak coupling, we set the Coulomb pseudopotential (μ^*) to 0.1.[41] We have calculated and consequently compared the superconductivity parameters of $(H_2)B_3C_3$ with the original SrB_3C_3 clathrate, as listed in Table 1. At 0 GPa, $(H_2)B_3C_3$ exhibits a lower ω_{log} (9.44 THz) compared to SrB_3C_3 (11.44 THz), attributable to its broader frequency spectrum stemming from the presence of high-frequency H–H vibrons (Figs. 4(a) and 4(b)), since ω_{log} is weighted heavily toward low-frequency phonons. The EPC in both structures predominantly arises from low- to mid-frequency vibrations of the B–C cages. While high-frequency vibrations of hydrogen atoms are generally favorable for enhancing EPC, in this case, the hydrogen retains its molecular form and contributes insignificantly to λ. The calculated λ value of 1.34 in $(H_2)B_3C_3$, compared to 1.02 in SrB_3C_3, can be attributed to the differences in the shapes and sizes of the clathrate cages in these two compounds. Balancing ω_{log} and λ, the estimated T_c for $(H_2)B_3C_3$ is 46.1 K, which is very close to the calculated T_c of 45 K for SrB_3C_3. The marginally higher T_c in $(H_2)B_3C_3$ is attributed to substituting a lighter element, hydrogen, instead of the Sr atoms, and slightly higher DOS at the Fermi level due to the lower degree of doping. At 2 GPa, the calculated T_c for $(H_2)B_3C_3$ increases to 48.18 K, primarily due to the slightly amplified λ under high pressure. In contrast, the T_c for SrB_3C_3 decreases with increasing pressure due to a decrease in ω_{log}, λ, and DOS at the Fermi level.[30] The effect of H_2 rotation on the electron–phonon coupling was also investigated. As depicted in Table S2, the λ was calculated to be 1.32 in a rotated orientation, slightly lower than the original by 0.02. This is largely due to the cage dynamics as the size of the B–C cage changes during the reorientation of the hydrogen molecule. The high-frequency vibrations of hydrogen atoms contribute insignificantly to λ because the hydrogen retains its molecular form. The slight reduction in λ results in a negligible decrease in T_c of 0.02%. From Fig. S7, there is a slight increase in the phonon density of states (PHDOS) and Eliashberg spectra function for $(H_2)B_3C_3$ compared to Fig. 4. The higher PHDOS arises from changes in the phonon spectrum due to the altered shape and size of the B–C cage. Therefore, the rotation of the molecular hydrogen has an insignificant effect on the electron–phonon coupling constant and the T_c.

Notably, very high T_cs were predicted for type-VII clathrates using binary guest metal atoms. Here, the distribution of different metal valences allows one to finely tune

the density of states at the Fermi level. To date, $KPbB_6C_6$ was predicted to have the highest transition temperature with $T_c \approx 88$ K and an average valance of +1.5. The electronic structure of $(H_2)B_3C_3$ can be thought of as a slightly electron-doped vacant cage system, and the introduction of partial H_2 occupancy might serve as an additional valuable tool for fine-tuning the DOS in combination with the cage occupation of guest metal(s) (e.g., $(H_2)SrB_6C_6$ would enable an average valence of roughly +1).

Table 1. Superconducting parameters of various clathrate structures calculated with $\mu^* = 0.1$.

Structures	Pressure (GPa)	Space group	ω_{log} (THz)	λ	T_c (K)
$(H_2)B_3C_3$	2	$P4_2/mmc$	10.96	1.22	48.18
$(H_2)B_3C_3$	0	$P4_2/mmc$	9.44	1.34	46.10
SrB_3C_3	0	Pm-3n	11.44	1.02	45.00

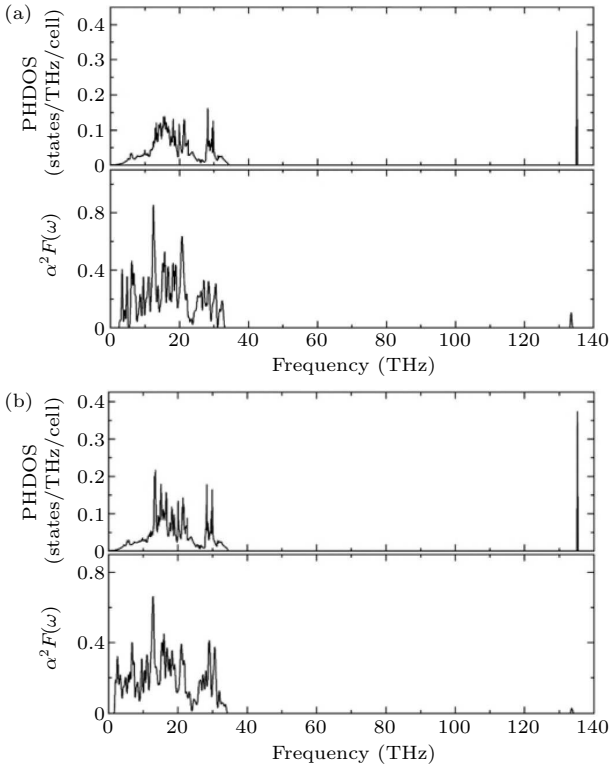


Fig. 4. Phonon density of states and Eliashberg spectra function for $(H_2)B_3C_3$ clathrate calculated (a) at atmospheric pressure and 0 K, and (b) at 2 GPa and 0 K.

It is worth noting that another class of hydrogen-based clathrate superconductors exhibit extremely high T_c under high pressure, with some even predicted to have T_c exceeding room temperature. This class includes materials such as LaH_{10},[7–10] CaH_6[69,70] and $YScH_6$.[71] However, these materials belong to the class of hydride superconductors, where their structural composition and the mechanisms governing superconducting properties differ significantly from those of B–C-caged superconductors like SrB_3C_3. In hydride superconductors, hydrogen forms clathrate cages that act as extended metallic hydrogen host structures stabilized by guest atoms, representing an intermediate state between molecular hydrogen and pure atomic hydrogen. The superconductivity of hydride superconductors is primarily driven by strong electron–phonon coupling mediated by hydrogen vibrations. This coupling is further enhanced by Fermi surface nesting and interactions between hydrogen and phonon modes, which substantially elevate the superconducting T_c.[71] In contrast, B–C-caged superconductors, such as SrB_3C_3, derive their superconducting properties mainly from the contributions of the B–C cages. These cages are more rigid around guest species, which in this case is molecular hydrogen. In the $(H_2)B_3C_3$ clathrate, hydrogen does not significantly contribute to the electron–phonon coupling.

4. Conclusion

In summary, we have systematically explored the electronic and superconducting properties of $(H_2)B_3C_3$ clathrate at ambient pressure and 2 GPa. The phonon dispersion curve reveals the dynamical stability of the structure at ambient conditions as well as a higher pressure of 2 GPa. The electron–phonon coupling calculations indicate that the $P4_2/mmc$ $(H_2)B_3C_3$ is a promising conventional superconductor with a calculated T_c of 46.1 K at ambient conditions. Compared with SrB_3C_3, substituting hydrogen atoms creates a novel structure with better electronic and increased superconducting properties. Our results advance the understanding of light-element clathrates under ambient conditions and encourage further investigations in the superconductivity research field.

Appendix A: Topological analysis of the electron density

A1. Electron localization function

To carry out the topological analysis and understand the interaction and bonding between H–H, B–H, and C–H in the $(H_2)B_3C_3$ structure, we have calculated the electron localization function (ELF). The electron localization function reveals the location of localized electrons, atomic shell structures, and electron localization in atomic and molecular systems. The electron localization D_σ can be measured as

$$D_\sigma = \tau_\sigma - \frac{1}{4}(\nabla\rho_\sigma)^2, \tag{A1}$$

where τ_σ is the kinetic energy density with spin σ. Since D_σ vanishes in one-electron systems or in regions of many-electron systems dominated by a single, localized spin orbital, it is more convenient to define an alternative ELF so that the inverse relationship between localization and D_σ can be fixed. The ELF can be written as

$$\mathrm{ELF} = \frac{1}{1+\left(\frac{D_\sigma}{D_\sigma^0}\right)^2}, \tag{A2}$$

where D_σ^0 represents the uniform electron gas.

An ELF isosurface in the $(H_2)B_3C_3$ clathrate with the isovalue $\eta = 0.75$ is depicted in Fig. A1. The result of the ELF calculation in the $(H_2)B_3C_3$ cage-like structure demonstrates the perfect overlap of the electron clouds of hydrogen atoms, indicating covalent bonding of the hydrogen atoms in the H_2 units. Also, an accumulation of localized electron pairs exists between B and C atoms. Furthermore, no electron localization between hydrogen and B–C cages suggests that the interaction should be closed shell in nature, in agreement with vdW interactions. The shortest B–H and C–H distances are 2.78 Å. These distances are slightly within the sum of the vdW radii of carbon (1.70 Å), boron (1.92 Å), and hydrogen (1.09 Å), suggesting that the presence of the right amount of hydrogen is vital to the formation of the stable compound. Furthermore, the nearest H–H distance was found to be 0.7166 Å, which is comparable to the H–H bond length of 0.74 Å in molecular hydrogen. At the slightly higher pressure of 2 GPa, these C–H, B–H, and H–H distances were reduced to 2.77 Å, 2.77 Å, and 0.7162 Å, respectively.

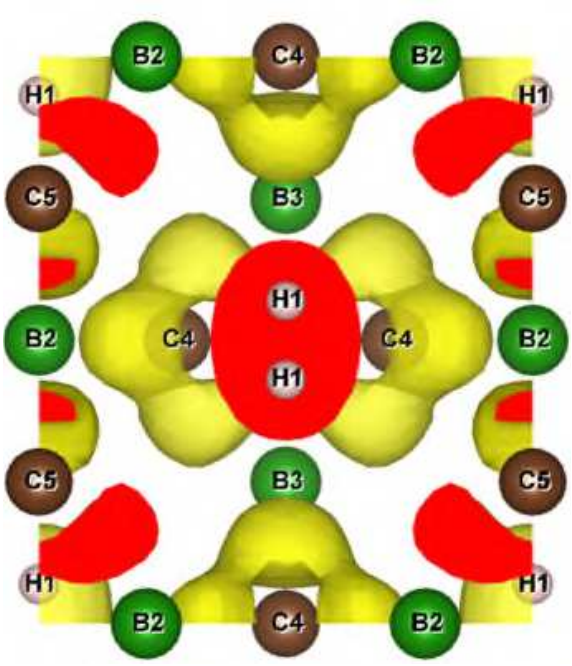


Fig. A1. Calculated electron localization function isosurface in $(H_2)B_3C_3$ crystal at ambient pressure $\eta = 0.75$. ELF is a dimensionless quantity ranging from 0 to 1. An ELF value of 1 corresponds to perfect localization, and a value of 0.5 corresponds to a free electron gas.

A2. Bond critical points between H···H, H···C, and B···C paths

Topological analysis of charge density at the bond critical point (BCP) was carried out by using the quantum theory of atoms in molecules (QTAIM)[52] as implemented in the CRITIC2 code.[63] Our calculation employed grid points of $80 \times 80 \times 512$ (at 0 and 2 GPa). In a periodic system, typically a solid, the number and types of critical points are determined by

$$n - b + r - c = 0, \;\; n, c \geq 1, \;\; b, r \geq 3, \tag{A3}$$

where n, b, r, and c represent the numbers of nuclei, bond, ring, and cage critical points. The QTAIM, as implemented in the CRITIC2, can be used to obtain topological properties from the calculation of the CPs, such as potential energy density $V(\boldsymbol{r})$, kinetic energy density $G(\boldsymbol{r})$, electron density $\rho(\boldsymbol{r})$, and its Laplacian $\nabla^2\rho(\boldsymbol{r})$ at a CP. The local form of the virial theorem relates the $V(\boldsymbol{r}_{\rm BCP})$ and the kinetic energy density $V(\boldsymbol{r}_{\rm BCP})$ to $\nabla^2\rho(\boldsymbol{r}_{\rm BCP})$,[72,73]

$$V(\boldsymbol{r}_{\rm BCP}) = \frac{\hbar^2}{4m}\nabla^2\rho(\boldsymbol{r}_{\rm BCP}) - 2G(\boldsymbol{r}_{\rm BCP}). \tag{A4}$$

For closed-shell interaction, a straightforward expression has been proposed to assess the $G(\boldsymbol{r}_{\rm BCP})$ from electron density distribution,[74]

$$G(\boldsymbol{r}_{\rm BCP}) = \frac{3}{10}(3\pi^2)^{\frac{2}{3}}\rho^{\frac{5}{3}}(\boldsymbol{r}_{\rm BCP}) + \frac{1}{6}\nabla^2\rho(\boldsymbol{r}_{\rm BCP}). \tag{A5}$$

The bond dissociation energy ($E_{\rm BD}$) can then be evaluated using the virial theorem, i.e.,

$$E_{\rm BD} = -\frac{1}{2}V(\boldsymbol{r}_{\rm BCP}). \tag{A6}$$

The topological properties of the electron density in the $(H_2)B_3C_3$ clathrate structure were calculated at 0 and 2 GPa, and are summarized in Tables A1 and A2, respectively. At both pressures, the topological analysis identifies BCPs between distinct carbon–hydrogen atoms, hydrogen–hydrogen atoms, and between boron and carbon atoms only. Notably, no BCPs were found between boron and hydrogen atoms at either 0 or 2 GPa, consistent with the attractor connectivity matrix for both pressures. The attractor connectivity matrix gives the number of bond paths between the different types of

Table A1. Topological properties at the BCPs for nearest neighboring H···H, H···C, and B···C contacts in the $(H_2)B_3C_3$ structure at 0 GPa. The multiplicity of the interaction is denoted by M, and D is the bond distance.

Type	D (Å)	M	$\rho(\boldsymbol{r}_{\rm BCP})$ (e^-·Å^{-3})	$\nabla^2\rho(\boldsymbol{r}_{\rm BCP})$ (e^-·Å^{-5})	G (kJ·mol^{-1})	V (kJ·mol^{-1})	$E_{\rm BD}$ (kJ·mol^{-1})
H1···H1	0.7166	2	2.0009	−41.1046	247.4667	−1614.5246	807.2623
H1···C5	2.7780	8	0.1155	1.4755	35.3685	−30.5470	15.2735
B2···C5	1.6149	8	1.0350	−2.6244	283.6330	−638.7482	319.3741
B3···C4	1.6241	8	1.0257	−3.7141	258.8791	−618.9210	309.4605
B2···C4	1.7792	8	0.7605	−4.8420	110.2834	−352.4502	176.2251

Table A2. Topological properties at the BCPs for nearest neighboring H···H, H···C, and B···C contacts in the $(H_2)B_3C_3$ structure at 2 GPa. The multiplicity of the interaction is denoted by M, and D is the bond distance.

Type	D (Å)	M	$\rho(\boldsymbol{r}_{\mathrm{BCP}})$ ($e^-\cdot$Å^{-3})	$\nabla^2\rho(\boldsymbol{r}_{\mathrm{BCP}})$ ($e^-\cdot$Å^{-5})	G (kJ·mol^{-1})	V (kJ·mol^{-1})	E_{BD} (kJ·mol^{-1})
H1···H1	0.7162	2	2.0042	−41.1571	249.3648	−1619.7334	809.8667
H1···C5	2.7709	8	0.1181	1.5037	36.1482	−31.3584	15.6792
B2···C5	1.6115	8	1.0406	−2.4098	290.5470	−646.7170	323.3585
B3···C4	1.6195	8	1.0332	−3.5738	265.2375	−627.8318	313.9159
B2···C4	1.7714	8	0.7694	−4.6774	117.1400	−361.6655	180.8328

non-equivalent atoms in the cell. Furthermore, the calculated attractor connectivity matrix indicates the absence of B···B and C···C bond paths.

Acknowledgments

This work was supported by Carnegie Canada and Natural Sciences and Engineering Research Council of Canada (NSERC). Calculations were performed using computing resources provided by the University of Saskatchewan, WestGrid, and Digital Research Alliance of Canada. TAS acknowledges support from the U.S. Department of Energy (DOE), Office of Science, Basic Energy Sciences, under Award No. DE-SC0020683.

References

[1] Schrieffer J R 1999 *Theory of Superconductivity* (Boca Raton: CRC Press)
[2] Onnes H K 1911 *Commun. Phys. Lab. Univ. Leiden* **12** 120
[3] Sun G F, Wong K W, Xu B R, Xin Y and Lu D F 1994 *Phys. Lett. A* **192** 122
[4] Duan D, Liu Y, Tian F, Li D, Huang X, Zhao Z, Yu H, Liu B, Tian W and Cui T 2014 *Sci. Rep.* **4** 6968
[5] Drozdov A P, Eremets M I, Troyan I A, Ksenofontov V and Shylin S I 2015 *Nature* **525** 73
[6] Einaga M, Sakata M, Ishikawa T, Shimizu K, Eremets M I, Drozdov A P, Troyan I A, Hirao N and Ohishi Y 2016 *Nat. Phys.* **12** 835
[7] Liu H, Naumov I I, Hoffmann R, Ashcroft N W and Hemley R J 2017 *Proc. Natl. Acad. Sci. USA* **114** 6990
[8] Peng F, Sun Y, Pickard C J, Needs R J, Wu Q and Ma Y 2017 *Phys. Rev. Lett.* **119** 107001
[9] Drozdov A P, Kong P P, Minkov V S, Besedin S P, Kuzovnikov M A, Mozaffari S, Balicas L, Balakirev F F, Graf D E, Prakapenka V B, Greenberg E, Knyazev D A, Tkacz M and Eremets M I 2019 *Nature* **569** 528
[10] Somayazulu M, Ahart M, Mishra A K, Geballe Z M, Baldini M, Meng Y, Struzhkin V V and Hemley R J 2019 *Phys. Rev. Lett.* **122** 027001
[11] Bardeen J, Cooper L N and Schrieffer J R 1958 *Phys. Rev. B* **108** 1175
[12] Pickard C J, Errea I and Eremets M I 2020 *Annu. Rev. Condens. Matter Phys.* **11** 57
[13] Bhattacharyya P, Chen W, Huang X, Chatterjee, Huang B, Kobrin B, Lyu Y, Smart T J, Block M, Wang E, Wang Z, Wu W, Hsieh S, Ma H, Mandyam S, Chen B, Davis E, Geballe Z M, Zu C, Struzhkin V, Jeanloz R, Moore J E, Cui T, Galli G, Halperin B I, Laumann C R and Yao N Y 2024 *Nature* **627** 73
[14] Sun Y, Lv J, Xie Y, Liu H and Ma Y 2019 *Phys. Rev. Lett.* **123** 097001
[15] Zhang Z, Cui T, Hutcheon M J, Shipley A M, Song H, Du M, Kresin V Z, Duan D, Pickard C J and Yao Y 2022 *Phys. Rev. Lett.* **128** 047001
[16] Dolui K, Conway L J, Heil C, Strobel T A, Prasankumar R P and Pickard C J 2024 *Phys. Rev. Lett.* **132** 166001
[17] Lilia B, *et al.* 2022 *J. Phys.: Condens. Matter* **34** 183002
[18] Eliashberg G 1960 *Sov. Phys.-JETP* **11** 696
[19] Eliashberg G 1961 *Sov. Phys.-JETP* **12** 1000
[20] Ashcroft N W 1968 *Phys. Rev. Lett.* **21** 1748
[21] Nagamatsu J, Nakagawa N, Muranaka T, Zenitani Y and Akimitsu 2001 *Nature* **410** 63
[22] McMillan W L 1968 *Phys. Rev.* **167** 331
[23] Zipoli F, Bernasconi M and Benedek G 2006 *Phys. Rev. B* **74** 205408
[24] Spagnolatti I, Bernasconi M and Benedek G 2003 *Euro. Phys. J. B* **34** 63
[25] Blasé X, Bustarret E, Chapelier C, Klein T and Marcenat C 2009 *Nat. Mater.* **8** 375
[26] Lu S, Liu H, Naumov I I, Meng S, Li Y, Tse J S, Yang B and Hemley R J 2016 *Phys. Rev. B* **93** 104509
[27] Jin S, Kuang S, Dou X, Hermann A and Lu C 2024 *J. Mater. Chem. C* **12** 1516
[28] Zeng T, Hoffmann R, Nesper R, Ashcroft N W, Strobel T A and Proserpio D M 2015 *J. Am. Chem. Soc.* **137** 12639
[29] Zhu L, Borstad G M, Liu H, Guńka P A, Guerette M, Dolyniuk J A, Meng Y, Greenberg E, Prakapenka V B, Chaloux B L, Epshteyn A, Cohen R E and Strobel T A 2020 *Sci. Adv.* **6** eaay8361
[30] Zhu L, Liu H, Somayazulu M, Meng Y, Guńka P A, Shiell T B, Kenney-Benson C, Chariton S, Prakapenka V B, Yoon H, Horn J A, Paglione J, Hoffmann R, Cohen R E and Strobel T A 2023 *Phys. Rev. Res.* **5** 013012
[31] Gai T T, Guo P J, Yang H C, Gao Y, Gao M and Lu Z Y 2023 *Phys. Rev. B* **105** 224514
[32] Strobel T A, Zhu L, Guńka P A, Borstad G M and Guerette M 2020 *Angew. Chem. Int. Ed.* **60** 2877
[33] Wang J N, Yan X W and Gao M 2021 *Phys. Rev. B* **103** 144515
[34] Di Cataldo S, Qulaghasi S, Bachelet G B and Boeri L 2022 *Phys. Rev. B* **105** 064516
[35] Zhang P, Li X, Yang X, Wang H, Yao Y and Liu H 2022 *Phys. Rev. B* **105** 094503
[36] Duan Q, Zhan L, Shen J, Zhong X and Lu C 2024 *Phys. Rev. B* **109** 054505
[37] Geng N, Hilleke K P, Zhu L, Wang X, Strobel T A and Zurek E 2023 *J. Am. Chem. Soc.* **145** 1696
[38] Cui X, Hilleke K P, Wang X, Lu M, Zhang M, Zurek E, Li W, Zhang D, Yan Y and Bi T 2020 *J. Phys. Chem. C* **124** 14826
[39] Li J, Yue J, Guo S, Zhang A, Zhu L, Song H, Liu L, Liu Y and Cui T 2024 *Phys. Rev. B* **109** 144509
[40] Ashcroft N W 2004 *Phys. Rev. Lett.* **92** 187002
[41] Sun Y and Zhu L 2024 *Commun. Phys.* **7** 324
[42] Hohenberg P and Kohn W 1964 *Phys. Rev.* **136** B864
[43] Kohn W and Sham L J 1964 *Phys. Rev.* **140** A1133
[44] Perdew J P, Burke K and Ernzerhof M 1996 *Phys. Rev. Lett.* **77** 3865
[45] Kresse G and Furthmüller J 1996 *Phys. Rev. B* **54** 11169
[46] Klimeš J, Bowler D R and Michaelides A 2011 *Phys. Rev. B* **83** 195131
[47] Blöchl P E 1994 *Phys. Rev. B* **50** 17953
[48] Car R and Parrinello M 1985 *Phys. Rev. Lett* **55** 2471
[49] Giannozzi P, Baroni S, Bonini N, *et al.* 2009 *J. Phys.: Condens. Matter* **21** 395502
[50] Troullier N and Martins J L 1991 *Phys. Rev. B* **43** 1993
[51] Nosé S 1984 *Mol. Phys.* **52** 255
[52] Bader R F W 1990 *Atoms in Molecules: A Quantum Theory* (Oxford: 725 Oxford University Press)
[53] Baroni S, de Gironcoli S, Dal Corso A and Giannozzi P 2001 *Rev. Mod. Phys.* **73** 515
[54] Togo A, Oba F and Tanaka I 2008 *Phys. Rev. B* **78** 134106
[55] Dynes R C 1972 *Solid State Commun.* **10** 615
[56] Allen P B and Dynes R C 1975 *Phys. Rev. B* **12** 905
[57] Momma K and Izumi F 2011 *J. Appl. Crystallogr.* **44** 1272
[58] Mao H K and Hemley R J 1994 *Rev. Mod. Phys.* **66** 671

[59] Yao Y and Klug D D 2012 *J. Phys.: Condens. Matter* **24** 265401

[60] Dopilka A, Childs A, Ovchinnikov A, Zhao R, Bobev S, Peng X and Chan C K 2021 *ACS Appl. Mater. Interfaces* **13** 42564

[61] Zurek E, Hoffmann R, Ashcroft N W, Oganov A R and Lyakhov A O 2009 *Proc. Natl. Acad. Sci. USA* **106** 17640

[62] Becke A D and Edgecombe K E 1990 *J. Chem Phys.* **92** 5397

[63] Otero-de-la-Roza A, Blanco M A, Martín Pendás A and Luaña V 2009 *Comput. Phys. Commun.* **180** 157

[64] Yao Y, Yong X, Tse J S and Greschner M J 2014 *J. Phys. Chem. C* **118** 29591

[65] Koch U and Popelier P L A 1995 *J. Phys. Chem.* **99** 9747

[66] Popelier P L A 1998 *J. Phys. Chem. A* **102** 1873

[67] Yao Y and Klug D D 2010 *Proc. Natl. Acad. Sci. USA* **107** 20893

[68] Simon A 1997 *Angew. Chem. Int. Ed.* **36** 1788

[69] Wang H, Tse J S, Tanaka K, Iitaka T and Ma Y 2012 *Proc. Natl. Acad. Sci. USA* **109** 6463

[70] Ma L, Wang K, Xie Y, Yang X, Wang Y, Zhou M, Liu H, Yu X, Zhao Y, Wang H, Liu G and Ma Y 2022 *Phys. Rev. Lett.* **128** 167001

[71] Shi L T, Si J G, Turnbull R, Liang A, Liu P F and Wang B T 2024 *Phys. Rev. B* **109** 054512

[72] Souhassou M, Lecomte C, Ghermani N-E, Rohmer M M, Wiest R, Benard M and Blessing R H 1992 *J. Am. Chem. Soc.* **114** 2371

[73] Espinosa E, Molins E and Lecomte C 1998 *Chem. Phys. Lett.* **285** 170

[74] Abramov Y A 1997 *Acta Crystallogr.* **A53** 264